Leveraging light-curve inversion for kinematic state estimation of uncooperative targets

LEVERAGING LIGHT-CURVE INVERSION FOR REAL-TIME KINEMATIC STATE ESTIMATION OF UNCOOPERATIVE TARGETS

Francesco Renis[1], Dr. Andrew Lawrence Price[2], Dr. Stephan Hellmich[3], Prof. Manuela Battipede[4], and Dr. Mathieu Salzmann[5]

[1] *Politecnico di Torino, 10129 Torino, Italy, Email: francesco.renis@studenti.polito.it*
[2] *EPFL CVLab, 1015 Lausanne, Switzerland, Email: andrew.price@epfl.ch*
[3] *EPFL LASTRO, 1290 Versoix, Switzerland, Email: stephan.hellmich@epfl.ch*
[4] *Politecnico di Torino, 10129 Torino, Italy, Email: manuela.battipede@polito.it*
[5] *EPFL CVLab, 1015 Lausanne, Switzerland, Email: mathieu.salzmann@epfl.ch*

ABSTRACT

The growing number of space objects threatens mission sustainability, making precise real-time tracking essential for Active Debris Removal (ADR) and In-Orbit Servicing (IOS) missions. For an uncooperative target, a Vision Based Navigation (VBN) relative pose (attitude and position) estimation system coupled with a state estimator are likely required. Missions can further be supported by commissioning unresolved observations of the target to produce light curves which can then be used to extract rotation rates and axes of rotation. This work performs the novel task of exploiting the light curves as kinematic priors to enhance the performance of the state estimator.

An Extended Kalman Filter (EKF) and an Unscented Kalman Filter (UKF) are implemented. Light curve motion prior extraction and VBN pose estimation are simulated. Three independent studies are performed exploiting the motion priors: (1) Optimizing the Kalman filter tuning for specific kinematic scenarios; (2) Injecting the priors as an initial condition to improve convergence and steady state errors; and (3) Enhancing an outlier rejection function with supplementary proxy measurements from the priors. Performance is evaluated on a custom synthetic light curve dataset based on the Atlas Centaur rocket body, and a private commercial dataset based on the Vega Secondary Payload Adapter from commercial collaborator, ClearSpace. Pose estimation results are simulated based on state-of-the-art machine learning spacecraft pose estimators.

By exploiting kinematic priors, convergence time and steady state error reductions of $3\times$ or more are exhibited for certain state components, dependent on the kinematic scenario and filter tuning. In general, several trade-offs are observed with kinematic priors providing the opportunity for the lowest steady state errors. This method has the potential to improve the pose estimation accuracy for proximity operations of uncooperative tumbling objects, supporting ADR and IOS missions, especially considering the mild assumptions required.

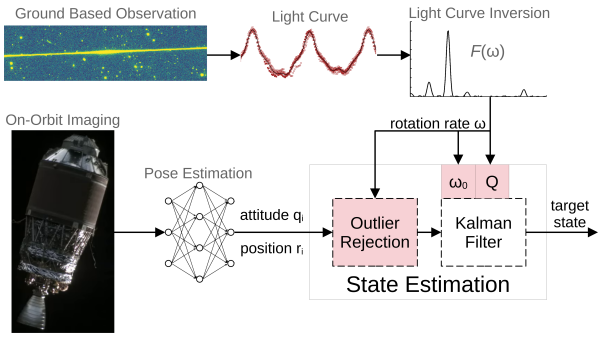

Figure 1. Project overview. Motion priors from previous ground observations are exploited to augment the performance of an on-orbit state estimator for an uncooperative target. Light curve visualization from [34]. Spacecraft visualization from [16].

Keywords: Active removal and serving; Light-curves; Measurements; State estimation; Kalman Filtering; ESA.

1. INTRODUCTION

As of the July 2024 space environment report, the ESA is tracking 20k+ objects in Low Earth Orbit (LEO) with modeled estimations of millions more untracked objects [10]. Currently, various programs are underway to support and develop the technologies necessary for active debris removal (e.g. ADRIOS and CRD2). This work is carried out in the context of a general in-orbit servicing or active debris removal mission.

For a non-functioning target satellite or piece of debris, a servicer satellite will not have access to cooperative relative navigation techniques such as relative GNSS, target telemetry or beacons. For relative attitude determination in such uncooperative circumstances, an optical sensing technique coupled with a state estimator such as a Kalman Filter is required.

In advance of a servicing mission, observations of the client satellite can be made using ground-based and in-orbit Space Situational Awareness (SSA) services. In particular, light curve observations can be contracted from several telescope networks to assess a satellite's operational status [30, 13]. Assuming the target's shape and reflective properties are known, it is possible to extract information about the target's kinematics. This extraction of kinematics information can then be passed to a state estimator as a kinematic prior (or "motion prior").

In this paper, the benefits of exploiting the motion prior for an uncooperative servicing mission are explored. The remaining paper sections are organized as follows. [2] **Related Works** are reviewed. [3] A **Relative Dynamics Model** is introduced to simulate both the target and servicer orbits, positions and attitudes. The [4] **State Estimation Model** is introduced. The choice of Kalman Filter is justified and the mathematical preliminaries of state estimation are provided. [5] **Light Curve Analysis** is reviewed. Limitations associated with single axis rotation and two axis rotation are discussed. [6] Results from the **Experiments** with the state estimation model exploiting motion priors are presented.

In particular, the advantages of exploiting motion priors are quantified in three studies as depicted in Figure 1.

1. With prior knowledge of the target, the state estimator parameters, Q, can be tuned for a specific kinematic state resulting in a lower steady-state error.

2. By incorporating the motion prior, ω_0 as an initial condition, the state estimator is able to converge earlier. This is especially evident when estimating the target inertia matrix for multi-access tumbling.

3. The motion prior can be used to augment measurement error outlier rejection algorithms.

2. RELATED WORK

This work focuses on a state estimation model which relies on inputs from light curves and relative pose (i.e., position and attitude) measurements. For uncooperative targets (i.e., no telemetry, visual markers or beacons), a VBN system is typically required for pose estimation. Here a brief review of uncooperative target spacecraft state estimation, Kalman filter implementations and light curve inversion techniques are reviewed.

2.1. Uncooperative Spacecraft Pose Estimation and State Tracking

The state-of-the-art for uncooperative spacecraft VBN is briefly reviewed here.

Sensor fusion from multiple independent sensors is standard practice for estimating the relative pose of spacecraft. In 2019, the Northropp Grumman Mission Extension Vehicle (MEV)'s VBN system included 6 visible spectrum cameras, four infrared cameras and a single scanning LIDAR [33]. The visible and infrared cameras included both narrow and wide Field of View (FoV) for long distance and proximity imaging respectively. The work was able to perform target classification and distance estimation in excess of 30 km. The system transitions to wide FoV cameras at approximately 15 m. The infrared system was used similarly with narrow FoV cameras in excess of 10 km and wide FoV cameras again at 15 m. The LIDAR provided rough scans at 2 km and was used throughout many phases of the mission. The computer vision feature extraction method and the state tracking algorithm were not explicitly shared.

In 2018, the RemoveDEBRIS mission demonstrated uncooperative capture of a target cubesat. The removeDEBRIS VBN system had two visible spectrum cameras and a LIDAR [11]. Mission planning explored chaser-target scenarios up to 500 m apart and state tracking was performed with an EKF [5]. A template matching VBN technique was employed for 3 DoF (i.e., position) navigation. For 6 DoF navigation, measurements are fused from the LIDAR and cameras. With the LIDAR 3 DoF - 3 DoF point cloud matching to a target CAD model is performed. With the cameras, first initialization is performed by extracting a silhouette from the images and compared against a hierarchical model view graph. Once initialization is complete, a frame by frame local edge tracking is performed similar to [8].

In 2018, the JAXA Hayabusa 2 mission visited the asteroid Ryugu and released the MinervaII-2 rover to the surface of Ryugu [14]. The Hayabusa 2 optical navigation camera system was equipped with two wide FoV cameras and a single narrow FoV camera [37]. JAXA used the narrow FoV camera to track the orbit insertion of the MinervaII-2 rover and compared the observed arc to orbit insertion Monte Carlo simulations to finally obtain the release velocity [26]. Additionally, an independent study similarly estimated the release velocity from initial images captured by one of the wide FoV cameras using a Convolutional Neural Network (CNN) [32].

Notably, the majority of in-orbit demonstrations have used conventional computer vision techniques such as edge detectors and template matching. However, the spacecraft pose estimation competitions hosted by ESA and the Stanford Space Rendezvous Laboratory yielded only machine learning based pose estimation algorithms as state-of-the-art [21, 29]. Companies such as Airbus and Clearspace are planning on in-orbit demonstrations of machine learning VBN.

From this context of uncooperative spacecraft pose estimation supplied as measurements to a state estimation algorithm, a simple measurement system consisting of an optical camera and a CNN pose estimation algorithm is proposed for this study. No sensor fusion is performed

here. Measurement errors proportional to the error rate of a deployable CNN [15, 35] are assumed.

2.2. Kalman Filter Implementations

The most used model for real-time state estimation is, notably, the Kalman Filter. Given some noisy measurements, it employs a two step prediction-update recursive algorithm, leveraging a dynamic model representation of the underlying physical system.

Among several spacecraft relative dynamics models, this work adopts the one in [4]. It references the model in [12], but re-derives the expressions in the Target's (the uncooperative object) body frame. This way, the only additional measurements required are the absolute states of the Servicer, which are available from its Attitude and Orbit Determination System AODS. Additionally, a Target's inertia matrix parametrization as the one proposed in [38] is included.

To ensure the quaternion unitary norm, Kalman Filter implementations addressing this constraint have been considered. The Extended Kalman Filter EKF, originally developed by R.E.Kalman [20] constitutes the easiest nonlinear Kalman Filter extension. In [38] they developed an EKF propagating attitude errors in a minimal three parameters rotation representation, that then reconstructs the quaternion at each iteration (Multiplicative EKF). However, for simplicity, an explicit normalization at each iteration can yield acceptable results.

The Unscented Kalman Filter, a nonlinear extension that did not require an explicit linearization was originally developed in [17]. It propagates via the Unscented Transform a set of points sampling the state estimation error covariance matrix through the actual nonlinear process model. An UnScented QUaternion Estimator (USQUE) was proposed in [7], handling the unitary norm quaternion constraint by propagating a set of attitude errors represented as vectors of Modified Rodrigues Parameters, with a very similar approach to [38]. While adaptive methods, like the one in [28] building on USQUE, improve the parameter tuning process, they increase computational complexity. Instead, this work is able to provide information for accurate Kalman Filter parameter tuning, favoring a slightly risk-adverse but lighter approach.

To mitigate divergence due to possibly non-Gaussian measurement noise, as happens during pose estimation neural network faults, robust filtering approaches have been explored. Among various techniques [22], the simplest outlier rejection method proposed in [31] has been implemented. By setting a validation gate around the innovation term, an incoming measurements can be tested for a desired confidence level.

2.3. Light Curve Analysis

Acquiring and examining series of brightness measurements, called light curves, is a very powerful technique to obtain additional characteristics of unresolved targets. Light curve analysis has many applications in astronomy, including determining rotation rates [39], shapes [18, 19], and taxonomic classification of solar system objects [27], characterizing exoplanets and extrasolar planetary systems [24] and variable stars [9].

Light curves contain extensive information on the dynamic and physical properties of satellites and orbital debris. The brightness variations are directly related to the rotation of the object and the observation geometry. Light curve analysis allows to determine the attitude of the observed object and provides important information for ADR and helps to model effects that influence the long-term dynamics of the object, such as the electromagnetic field, drag, solar radiation, fuel sloshing or outgassing. The most frequently used methods to extract the apparent (synodic) period from the light curves are Fourier-based techniques. A comprehensive review on the analysis techniques of optical measurements from space objects is given in [36]

In this work, we apply the Fourier transform and CLEAN algorithm (WindowCLEAN). This method was developed to characterize the complex rotation of asteroids and comets in the solar system [23, 1, 25] and can reliably detect the dominant frequencies in light curves obtained from non-principal axis rotators. It was suggested that combining the periodicity analysis of light curves with WindowCLEAN with the shape inversion of radar observations may be a powerful tool to deduce non-principal axis spin states by significantly reducing the spin state parameter space that the shape inversion algorithm has to search [25]. This is why we selected WindowCLEAN to extract the kinematic priors for the state estimation.

3. RELATIVE DYNAMICS MODEL

In this section a model for the description of two spacecrafts' relative motion is presented. Consider two rigid-body spacecrafts orbiting around the earth, label one spacecraft as the Target, the uncooperative object in our context, and the other as the Servicer. For the chosen representation from [4], the relative translational dynamics is dependent on the relative attitude dynamics, which will be presented first.

Let $\mathfrak{q}_{TS} = \mathfrak{q}_S^{-1} \otimes \mathfrak{q}_T$ be the quaternion error between the attitude of the Target $\mathfrak{q}_T$ and the attitude of the Servicer $\mathfrak{q}_S$, representing the relative orientation between the two. The equivalent rotation matrix $R_S^T = R(\mathfrak{q}_{TS})$ transforms a vector expressed in the Servicer's body frame to the Target's body frame.

The relative angular velocity expressed in the Target

frame is given as:

$$\omega_{ST}^T = \omega_S^T - \omega_T^T = \mathbf{R}_S^T \omega_S^S - \omega_T^T \tag{1}$$

knowing that $\omega_{ST}^T = -\omega_{TS}^T$. Relative attitude and relative angular velocity follow the quaternion kinematics equation as:

$$\mathbf{q}_{TS} = \frac{1}{2} Q(\mathbf{q}_{TS}) \omega_{TS}^T \tag{2}$$

where

$$Q(\mathbf{q}) \doteq \begin{bmatrix} -q_1 & -q_2 & -q_3 \\ q_0 & -q_3 & q_2 \\ q_3 & q_0 & -q_1 \\ -q_2 & q_1 & q_0 \end{bmatrix} \tag{3}$$

The relative angular acceleration is expressed as:

$$\begin{aligned} \alpha_{ST}^T &= \left(\left. \frac{d\omega_{ST}}{dt} \right|_T \right)^T \\ &= \mathbf{R}_I^T \left(\left. \frac{d\omega_{ST}}{dt} \right|_I \right)^I - \omega_T^T \times \omega_{ST}^T \end{aligned} \tag{4}$$

where the subscripts after the vertical bar represent in which reference frame the differentiation is done, I is the Earth Centered Inertial (ECI) frame, and $\mathbf{R}_I^T$ is the rotation matrix that transforms a vector from the ECI frame into the Target frame, represented by the Target's attitude.

The expression of the relative angular acceleration with respect to the ECI frame, differentiated in the ECI frame, is computed as:

$$\left(\left. \frac{d\omega_{ST}}{dt} \right|_I \right)^I = \left(\left. \frac{d\omega_S}{dt} \right|_I \right)^I - \left(\left. \frac{d\omega_T}{dt} \right|_I \right)^I \tag{5}$$

Knowing that:

$$\begin{aligned} \mathbf{R}_I^T \left(\left. \frac{d\omega_T}{dt} \right|_I \right)^I &= \left(\left. \frac{d\omega_T}{dt} \right|_T \right)^T \\ &= \mathbf{J}_T^{-1} \left(\mathbf{m}_T - \omega_T^T \times \mathbf{J}_T \omega_T^T \right) \\ \mathbf{R}_I^T \left(\left. \frac{d\omega_S}{dt} \right|_I \right)^I &= \mathbf{R}_S^T \left(\left. \frac{d\omega_S}{dt} \right|_S \right)^S \\ &= \mathbf{R}_S^T \left[\mathbf{J}_C^{-1} \left(\mathbf{m}_C - \omega_S^S \times \mathbf{J}_S \omega_S^S \right) \right] \end{aligned} \tag{6}$$

where $\mathbf{J}_T$ and $\mathbf{J}_S$ are respectively the inertia matrices of the Target and of the Servicer, and $\mathbf{m}_T$ and $\mathbf{m}_S$ are respectively external moments applied to the Target and to the Servicer (assumed zero), the final expression for the relative angular acceleration then becomes:

$$\begin{aligned} \alpha_{ST}^T = \mathbf{R}_S^T &\left[\mathbf{J}_S^{-1} \left(\mathbf{m}_S - \omega_S^S \times \mathbf{J}_C \omega_S^S \right) \right] \\ &- \mathbf{J}_T^{-1} \left(\mathbf{m}_T - \omega_T^T \times \mathbf{J}_T \omega_T^T \right) - \omega_T^T \times \omega_{ST}^T \end{aligned} \tag{7}$$

The relative dynamics description is instead computing starting from the expressions of $\mathbf{r}_T^T$ and $\mathbf{r}_S^S$, which are, respectively, the Target's and Servicer's position expressed in their respective body frames. The relative position is defined as:

$$\mathbf{r}_{ST}^T = \mathbf{r}_S^T - \mathbf{r}_T^T = \mathbf{R}_S^T \mathbf{r}_S^C - \mathbf{r}_T^T \tag{8}$$

The relative velocity expressed in the target frame is obtained as:

$$\mathbf{v}_{ST}^T = \left(\left. \frac{d\mathbf{r}_{ST}}{dt} \right|_T \right)^T = \left(\left. \frac{d\mathbf{r}_{ST}}{dt} \right|_I \right)^T - \omega_T^T \times \mathbf{r}_{ST}^T, \tag{9}$$

$$= \mathbf{R}_S^T \mathbf{R}_I^S \left(\left. \frac{d\mathbf{r}_{ST}}{dt} \right|_I \right)^I - \left(\mathbf{R}_S^T \omega_S^S - \omega_T^T \right) \times \mathbf{r}_{ST}^T. \tag{10}$$

developed using Eq. (1).

The relative acceleration in the Target frame is computed as:

$$\begin{aligned} \mathbf{a}_{ST}^T &= \left(\left. \frac{d^2\mathbf{r}_{ST}}{dt^2} \right|_T \right)^T \\ &= \left(\left. \frac{d^2\mathbf{r}_{ST}}{dt^2} \right|_I \right)^T - 2\omega_T^T \times \mathbf{v}_{ST}^T \\ &+ \left(\left. \frac{d\omega_T}{dt} \right|_T \right)^T \times \mathbf{r}_{ST}^T + \omega_T^T \times \left(\omega_T^T \times \mathbf{r}_{ST}^T \right) \end{aligned} \tag{11}$$

The relative acceleration term expressed in the Target frame, differentiated with respect to the ECI frame is simply corresponding to:

$$\left(\left. \frac{d^2\mathbf{r}_{ST}}{dt^2} \right|_I \right)^T = \left(\left. \frac{d^2\mathbf{r}_S}{dt^2} \right|_I \right)^T - \left(\left. \frac{d^2\mathbf{r}_T}{dt^2} \right|_I \right)^T \tag{12}$$

The absolute accelerations of the Target and the Servicer with respect to the ECI frame are:

$$\left(\left. \frac{d^2\mathbf{r}_S}{dt^2} \right|_I \right)^T = -\frac{\mu}{r_S^3} \mathbf{R}_S^T \mathbf{r}_S^S \tag{13}$$

$$\begin{aligned} \left(\left. \frac{d^2\mathbf{r}_T}{dt^2} \right|_I \right)^T &= -\frac{\mu}{r_T^3} \mathbf{r}_T^T \\ &= -\frac{\mu}{\|\mathbf{R}_S^T \mathbf{r}_S^S - \mathbf{r}_{ST}^T\|^3} (\mathbf{R}_S^T \mathbf{r}_S^S - \mathbf{r}_{ST}^T). \end{aligned} \tag{14}$$

which correspond to the standard Keplerian orbit propagation derived from the free restricted two body equation. By substituting Eqs. (12), (13) and (14) into Eq. (11), the complete expression of the relative translational dynamics expressed in the Target's body frame yields:

$$\begin{aligned} \mathbf{a}_{ST}^T = &-\frac{\mu}{r_S^3} \mathbf{R}_S^T \mathbf{r}_S^S \\ &+ \frac{\mu}{\left\| \mathbf{R}_S^T \mathbf{r}_S^S - \mathbf{r}_{ST}^T \right\|^3} \left(\mathbf{R}_S^T \mathbf{r}_S^S - \mathbf{r}_{ST}^T \right) \\ &+ \mathbf{J}_S^{-1} \left(\mathbf{m}_S - \omega_S^T \times \mathbf{J}_S \omega_S^T \right) \times \mathbf{r}_{ST}^T \\ &- 2\omega_S^T \times \mathbf{v}_{ST}^T + \omega_S^T \times \left(\omega_S^T \times \mathbf{r}_{ST}^T \right) \end{aligned} \tag{15}$$

The complete dynamics of the spacecraft relative motion problem, expressed in state-space representation, thus propagates as follows:

$$\dot{\mathbf{x}} = \left.\frac{d\mathbf{x}}{dt}\right|_T = \frac{d}{dt}\begin{bmatrix} \mathbf{q}_{TS} \\ \omega_{ST}^T \\ \mathbf{r}_{ST}^T \\ \mathbf{v}_{ST}^T \end{bmatrix}_{|T} = \begin{bmatrix} \frac{1}{2}\mathbf{Q}(\mathbf{q})\omega_{TS}^T \\ \alpha_{ST}^T \\ \mathbf{v}_{ST}^T \\ \mathbf{a}_{ST}^T \end{bmatrix} \tag{16}$$

As stated in the introduction, all the description is presented in its most general form. At the same time, it provides also the expressions that allow to derive a representation solely dependent on relative states and absolute states of the Servicer, which will be needed later during the discussion.

3.1. Software framework

The principal simulation environment has been designed in MATLAB/Simulink version R2019b. All the integrations are performed using the *ode4* integration method with fixed simulation sampling time of 0.01 seconds. The integrations inside the Kalman Filter exploit the same *ode4* integration method with the fixed filter sampling time defined before each case study.

4. STATE ESTIMATION MODEL

This chapter introduces the state estimation framework used in this study.

The state estimation model internally reference the spacecraft relative dynamics model presented in Section 3. In particular, the following state vector is defined:

$$\mathbf{x} = \begin{bmatrix} \mathfrak{q}_{TS} & \omega_{ST}^T & \mathbf{r}_{ST}^T & \mathbf{v}_{ST}^T & \mathbf{J}_T^k \end{bmatrix}^{\mathrm{T}} \tag{17}$$

The first 4 components, for a total vector of dimensionality in $\mathbb{R}^{13}$, correspond exactly to the 4 relative attitude and relative translational dynamics components from Eq. (16). The last state component $\mathbf{J}_T^k$ refer to a parametrization of the Target's inertia matrix, to possibly enable its estimation in some scenarios. The following parametrization from [38] is used:

$$J_T^k = \begin{bmatrix} J_x/J_y & 0 & 0 \\ 0 & 1 & 0 \\ 0 & 0 & J_z/J_y \end{bmatrix} = \begin{bmatrix} e^{k_1} & 0 & 0 \\ 0 & 1 & 0 \\ 0 & 0 & e^{-k_2} \end{bmatrix} \tag{18}$$

where J_x, J_y, J_z are the elements on the diagonal and the two parameters whose fixed values are:

$$\begin{aligned} k_1 &= \ln(J_x/J_y) \\ k_2 &= \ln(J_y/J_z) \end{aligned} \tag{19}$$

are estimated during the process. The Target's inertia matrix can thus only be estimated up to a scale factor, which represents the third missing degree of freedom. The Euler equations that appear in the dynamics model, however, yield the same result regardless.

This estimated inertia matrix is used as the Target's inertia matrix J_T inside the estimation process. Being constant, the inertia matrix parameters have no dynamics. Thus, with

$$\dot{\mathbf{J}}_T^k = \begin{bmatrix} \dot{k}_1 \\ \dot{k}_2 \end{bmatrix} = \mathbf{0} \tag{20}$$

the complete process dynamics used inside the estimator becomes:

$$\dot{\mathbf{x}} = \left.\frac{d\mathbf{c}}{dt}\right|_T = \frac{d}{dt}\begin{bmatrix} \mathbf{q}_{TS} \\ \omega_{ST}^T \\ \mathbf{r}_{ST}^T \\ \mathbf{v}_{ST}^T \\ \mathbf{J}_T^k \end{bmatrix}_{|T} = \begin{bmatrix} \frac{1}{2}\mathbf{Q}(\mathbf{q})\omega_{TS}^T \\ \alpha_{ST}^T \\ \mathbf{v}_{ST}^T \\ \mathbf{a}_{ST}^T \\ \mathbf{0} \end{bmatrix} \tag{21}$$

for a total dimensionality in $\mathbb{R}^{15}$.

In this work, an Extended Kalman Filter and an Unscented Kalman Filter implementation have been developed to serve as real-time state estimation models. Since quaternions are used for attitude representation, maintaining their unit norm is crucial to prevent errors in rotation, loss of physical validity, and drift in estimated states. Norm deviations arise from operations outside quaternion space, with error accumulation depending on how often such violations occur.

Consider the discrete-time autonomous (no external input) nonlinear system:

$$x_{k+1} = f(x_k) + d_k \tag{22}$$

$$y_k = h(x_k) + d_k^y \tag{23}$$

where $k \in \mathbb{Z}$ is the time index, $x_k \in \mathbb{R}^n$ is the state, $y_k \in \mathbb{R}^m$ is the measured output, d_k is the process noise and d_k^y is the measurement noise. Assume that both d_k and d_k^y are independent and identically distributed and white noises, zero mean with bounded variance. Eq. (22) is called *process model*, and references the relative dynamics model presented inside the Kalman Filters. Eq. (23) is called *measurement model*, it's the same for the two filters and, as already introduced, is simply defined as:

$$h(x_k) = \begin{bmatrix} \mathfrak{q}_{TS} \\ \mathbf{r}_{ST}^T \end{bmatrix} \tag{24}$$

The first two section describes the Kalman Filter implementations, with the respective strategies to handle the quaternion normalization constraint. After, a description of the measurement model and their real-time simulation is presented.

4.1. Extended Kalman Filter

The idea behind the EKF, the easiest extension of the Linear Kalman Filter, is to work with the linearized system

around the estimated state trajectory. That is, at each time step, compute:

$$\begin{aligned} F_k &= \frac{\partial f}{\partial x}(\hat{x}_k) \\ H_k &= \frac{\partial h}{\partial x}(\hat{x}_k) \end{aligned} \tag{25}$$

where F_k is the Jacobian of the relative dynamics process model f evaluated at $(\hat{x}_k, u_k)$ and H_k is the Jacobian of h evaluated at $(\hat{x}_k)$. The estimation procedure is thus linear and of relatively simple implementation. It is based on the two steps described below:

1. *Prediction*
   Knowing the estimated state of the system at time $k-1$, the filter computes a prediction of the state $\hat{x}_k^-$ using the system model and of the error covariance matrix P_k^-

$$\begin{aligned} x_k^- &= f(\hat{x}_{k-1}, u_{k-1}) \\ P_k^- &= F_{k-1} P_{k-1} F_{k-1}^T + Q_d \end{aligned} \tag{26}$$

2. *Update*
   The filter then uses the current output measurement y_k to build the innovation term δy_k and obtain the corrected estimate $\hat{x}_k$ and error covariance matrix P_k.

$$\begin{aligned} \hat{x}_k &= \hat{x}_k^- + K_k \delta y_k \\ \delta y_k &= y_k - H_k \hat{x}_k^- \\ S_k &= H_k P_k^- H_k^T + R_d \\ K_k &= P_k^- H_k^T S_k^{-1} \\ P_k &= (I - K_k H_k) P_k^- \end{aligned} \tag{27}$$

   where K_k is the Kalman gain matrix. The quaternion portion of the state estimate is then explicitly normalized:

$$\hat{\mathfrak{q}}_k = \frac{\hat{\mathfrak{q}}_k}{\|\hat{\mathfrak{q}}_k\|} \tag{28}$$

The Q_d and R_d matrices, respectively the process noise covariance matrix and measurement noise covariance matrix, are mostly designed offline and subject to tuning. Their values, for each state component, embed the confidence that is given on the model of the process and on the quality of the measurements (lower value, higher confidence) and have an impact on the convergence time and the amplitude of the oscillations at steady state (lower value, less oscillations but slower convergence). Typically, they are chosen as diagonal matrices with the variances of d_k and d_k^y on the diagonal. Such values can be modeled from prior understanding of the environment, and usually require trial and error tuning procedures.

Another parameter of a Kalman Filter is its sampling frequency $f_S = 1/\tau_S$. While analytical computations set a minimum value, it is usually constrained by the one of slowest processing unit in the real pipeline implementation. The value of the sampling rate, intuitively, has quite a big impact on the performance of the estimation process, both in terms of accuracy and convergence time.

Final relevant role in the process is played by the chosen initializations of the estimated variables, $\hat{x}_0$ and P_0. If a priori information on the system is available, the initial value of P_0 shall reflect the associated confidence (lower value, higher confidence), and a performance improvement can be expected. The two are set to $\mathbf{0}$ ad I_n otherwise.

With the relevant drawback associated to the computation of the Jacobians, that might need numerical derivation, the EKF has demonstrated to be effective for applications where models have low nonlinearities. The relative navigation scenario outlined in this work can arguably be the case.

4.2. Unscented Kalman Filter

The UKF is another extension of the Kalman Filter for nonlinear systems. Consider the same discrete-time nonlinear system in Eq. (22), with the same noise distribution assumptions.

The core process behind the UKF is, at each step, to generate a set of points, called Sigma Points, that sample that distribution of the state estimate. Those are then propagated individually through the nonlinear model (Unscented Transform), and then the distribution of such points is rebuilt, thus retrieving the new state estimate. In particular, the implementation uses attitude errors represented as a three-dimensional Modified Rodrigues Parameters vectors to be used inside the computations, as proposed in [7]. This way, a quaternion is never explicitly used in operations outside of its space, but an equivalent quaternion sigma points is still kept and propagated trough the process model.

Owing to space limitations, for the complete description of the model the reader might refer to [7].

A key addition lies in the handling of the incoming measurements. In particular, the quaternion error between between the incoming measurement $\tilde{y}_k^{\mathfrak{q}}$ and the propagated quaternion of the latest state estimate sigma point $\hat{\mathfrak{q}}_k^-(0)$ is computed and converted to MRP via the transformation defined in the cited source. The innovation term $v_k^{\delta \boldsymbol{p}}$ is thus computed as:

$$\delta\tilde{\boldsymbol{p}}_k = \delta\tilde{\mathfrak{q}}_k|_{MRP} = \left[\tilde{y}_k^{\mathfrak{q}} \otimes \left(\hat{\mathfrak{q}}_k^-(0)\right)^{-1}\right]_{|MRP} \tag{29}$$

$$v_k^{\delta \boldsymbol{p}} = \delta\tilde{\boldsymbol{p}}_k - \hat{y}_k^{-,\delta \boldsymbol{p}} \tag{30}$$

The update steps are then computed regularly.

The same reasoning for parameter tuning process as in the EKF holds here, keeping in mind the dimensionality 3 of the attitude component due to the error MRP representation used.

Among the advantages of the UKF with respect to the EKF there are lower expected errors and validity for higher-oder expansions. The principal drawbacks are usually higher computational costs and a more complex tuning process.

4.3. Outlier rejection

As stated, a robust filtering technique consisting of a simple outlier rejection mechanism, as proposed in [31] has been included in this work.

A validation gate is set around the innovation term using the normalized estimation error squared:

$$e_k^2 = v_k^T S_k^{-1} v_k \tag{31}$$

where v_k is the innovation term and S is the innovation covariance matrix (P_k^{vv} for a UKF). The innovation covariance weights the validation gate with the filter's trust in the measurement, preventing unnecessary rejection due to, for example, convergence being in progress.

Since e_k^2 follows a Chi-Squared (χ^2) distribution with m degrees of freedom, a hypothesis test determines whether to accept or discard a measurement. The Chi-Squared distribution, defined as:

$$Y = \sum_{i=1}^{k} \left(\frac{X_i - \mathbb{E}[X_i]}{\sigma} \right)^2 \tag{32}$$

measures how much a value deviates from expectations, higher values indicate larger deviations.

To test a measurement at confidence level α, the Kalman Filter checks whether e_k^2 lies within (χ_L^2, χ_U^2). These boundaries are computed as the inverse of the Chi-Squared cumulative distribution function with m degrees of freedom at $\frac{\alpha}{2}$ and $1 - \frac{\alpha}{2}$.

If a measurement is detected as faulty, the filter skips the update step, relying only on state prediction. When measurements originate from multiple sources, the outlier rejection mechanism is applied individually to each portion of the measurement vector. This requires defining individual update execution flows, where each update step maintains a covariance matrix R_d restricted to the non-faulty measurements, following the standard update steps.

This technique effectively detects measurement faults, provided they are temporary. Extended or frequent faults prevent measurement updates, leading the filter to diverge.

4.4. Real-time measurements model

As previously mentioned, the state estimation models introduced in this work rely on real-time measurements from a pose estimation model operating on proximity images. The available measurements consist of the relative orientation, represented as a quaternion, and the relative distance, defining the measurement model in Eq. (24)

Since the relative dynamics model directly solves for position and orientation, which are both states in the Kalman Filters, the measurement model remains linear, contributing to improved filter robustness.

The additional measurements required for process model integration are the absolute states $\mathbf{r}_S^S$ and ω_S^S of the Servicer, which are provided by its Attitude and Orbit Determination System. If the representation was instead derived with respect to the Servicer, the filters would need the absolute states of the Target, which are unavailable due to its assumed uncooperative nature.

This work is developed in a simulated environment that individually integrates torque-free attitude dynamics and Keplerian orbits for both the Servicer and the Target. The real-time measurements from the pose estimation model are thus simulated as the relative attitude and distance states, with added noise, and fed at a fixed Kalman Filter sampling frequency $f_s = 1/\tau_s$.

Quaternion noise is modeled using a rotation vector with a Gaussian-distributed random amplitude α_n (zero mean, variance $\sigma_y^{\mathfrak{q}}$) and a uniformly distributed random axis $\mathbf{r}_n$ on the unit sphere. The resulting noisy quaternion measurement is computed as:

$$\mathfrak{q}_n = \mathfrak{q} \otimes \delta\mathfrak{q}_n \tag{33}$$

where $\mathfrak{q}$ is the ground truth relative attitude, and $\delta\mathfrak{q}_n$ is obtained from the random rotation vector:

$$\delta\mathfrak{q} = \begin{bmatrix} \cos\left(\frac{\alpha_n}{2}\right) & \mathbf{r}_n \sin\left(\frac{\alpha_n}{2}\right) \end{bmatrix} \tag{34}$$

Relative distance noise is modeled as a three-dimensional random vector whose norm follows a zero-mean Gaussian distribution with variance σ_y^r. The quaternion angle noise variance $\sigma_y^{\mathfrak{q}} = 0.12$ rad and relative distance noise variance $\sigma_y^r = 0.37$ m are derived from real pose estimation results at a distance of 50 m.

Faulty measurements are modeled as highly noisy values to mimic the instability of relative pose and relative distance measurements during fault windows.

5. LIGHT CURVES ANALYSIS

The goal of this section is to briefly present some light curves analysis results to justify the assumed quality of the kinematic priors used in this work.

As presented in Section 2.3, the WindowCLEAN method has been implemented. Given the brightness samples of a light curve, the algorithm produces a *dirty* spectrum of the periodicities latent in the observations through a discrete Fourier transform that is then iteratively *cleaned* from aliases and unpredictable spurious periodicities.

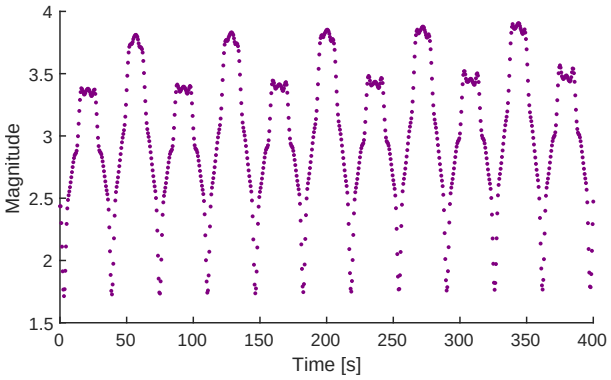

Figure 2. Synthetic Light Curve of an Atlas Centaur R/B. One axis tumbling, 5 deg/s

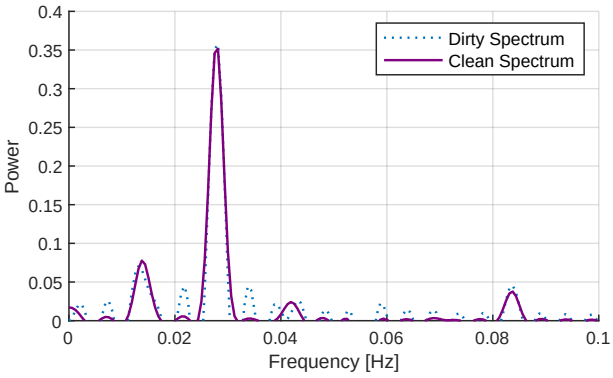

Figure 3. Spectrum of a synthetic Light Curve of an Atlas Centaur R/B. One axis tumbling, 5 deg/s

5.1. Single Axis Rotation

Extracting motion priors from an object in space rotating about a single axis is relatively straightforward. The period extracted by means of the frequency analysis directly corresponds to the synodic period and is interpreted as the rotation rate of the object that generated the light-curve.

In this context, the main issue lies in the scarce availability of light curves and related ground truth attitude data to effectively enable validation of the analyses.

Thanks to Luís Gonçalves, a PhD student from University of Coimbra, we had the opportunity to have access to a Lightcurve Simulator tool under his development. Based on an orbit integrator paired with the Cook-Torrance reflection model [6], it is able to generate a synthetic light curve generated by a given object model observed during a specified time window. As the implementation currently stands, the tumbling integration only supports one axis rotation with constant speed scenarios, and no additional simulated noise is included.

Below, a result on synthetic data is shown, with an additional case studied in collaboration with the commercial partner ClearSpace.

Synthetic data

An example of a synthetically generated light curve is presented in Fig. 2. It is produced by the simulated tumbling motion of an Atlas Centaur Rocket Body model, similar to the one proposed in [2]. The body is rotating about its z axis, aligned with its shorter dimension, observed for a time window of 400 seconds with a sampling time of 0.5 seconds.

The WindowCLEAN tool ran on this light curve is able to recover the clean spectrum shown in Fig. 3.

The extracted spectrum has the highest component at frequency 0.028 Hz, which corresponds to a period of around 35 seconds. Inspecting the nature of the light curve, exhibiting peaks at different magnitudes values, one can infer that the two different magnitude peaks are not generated by the same reflecting surface of the body. The resulting frequency corresponds thus to half the turns of the rocket body, whose two ends produce different brightness values. The recovered rotation rate, associated to half the extracted period, thus corresponds to 5.04 deg/s. For a ground truth constant rotation rate of 5 deg/s, the obtained precision is 99%.

Commercial data

We had the opportunity to validate our work on commercial data from our industry partner Clearspace. We had access to a generated light curve based on high fidelity synthetic ground based observations of a tumbling VEga Secondary Payload Adapter, corresponding to the one currently left in Low Earth Orbit after a launch in 2013.

We are unfortunately unable to share the raw brightness data, but the motion prior extraction process executed with our tool results in the recovered frequency spectrum shown in Fig. 4.

The commercial light curve accessed is 550 seconds long, with a sampling time of 1 s. The highest and most relevant frequency component is detected at 0.0082 Hz, which leads to a rotation rate of around 2.9 deg/s. Given the available ground truth value of 3 deg/s, the resulting precision is around 97%.

5.2. Two or Three Axis Rotation

While challenging, light curves scientific literature shows that it is possible to extract rotation rates for object rotating about a non trivial axis, resulting from superposition of motion about multiple body-fixed axes. In particular, accounting for the axis precession period requires knowledge of the targets body geometry, which cannot be al-

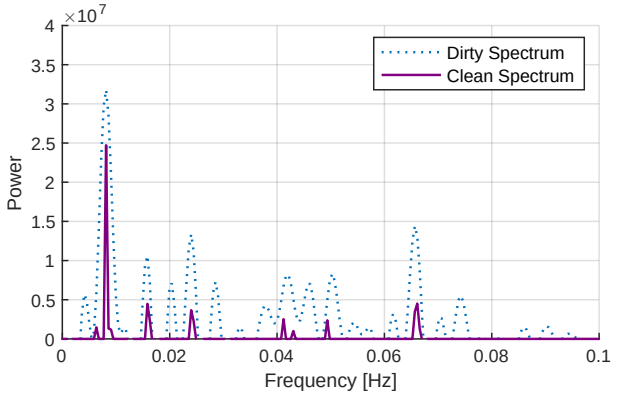

Figure 4. Spectrum of a Light Curve of a VESPA commercial model. One axis tumbling, 3 *deg/s*

ways assumed for an uncooperative target. Moreover, assuming a rotation rate can be extracted, enabling the motion prior injection as initial condition for the State Estimator would require adjusting for phase, due to the time shift between the light curve observation and the actual proximity operation with the Target.

5.3. Motion Prior Extraction Assumption

For the following experiments, we assume that motion priors are obtainable for both single axis and multi-axes tumbling cases. Specifically, we assume a conservative motion prior rotation rate extraction error of 5% relative to the ground truth rotation rates, based on our results from 5.1. In addition, a real Active Debris Removal mission would likely be planned to target an object that has been observed for a long time and exhibits a stable and safe motion. Therefore, assuming non-complex target tumbling, hence a trivial light curve analysis process, is thus justified for this reason as well.

6. KINEMATIC PRIOR INJECTION STUDIES

The experiments are organized into three studies demonstrating independent advantages of exploiting motion priors for state estimation as depicted in Figure 1.

- **Study 1 - Kalman Filter parameter tuning.** With a good initial estimate of the kinematics state, the Kalman filter parameters can be specifically tuned (e.g., tuning for a fast vs a slow rotation will enable a quicker convergence or lower steady state error).
- **Study 2 - Inertia matrix estimation improvement.** A kinematic prior can be directly injected as an initial condition for the Kalman filter.
- **Study 3 - Enhanced outlier rejection.** In challenging pose estimation scenarios such as during an eclipse, a kinematic prior may be injected as a proxy measurement to mitigate filter divergence.

Experimental Conditions

For the following experiments, the target is assumed to be a rocket body (e.g., the Atlas Centaur or the Japanese H2A). A representative principle inertia matrix, $J_T^k = diag(4.33, 1, 4)$, is used as defined by the parameterization of equation (18) with $k_1 = 1.466, k_2 = -1.439$.

The simulation length T_{sim} and the sampling time τ_s are defined before each case study. Unless specifically stated, the state variable is initialized with relative position r_0, velocity v_0, attitude q_0, and rotation rate ω_0 set to $\vec{0}$ and the target inertia matrix, $J_{T,0}^k = J_T^k \circ [a_0, a_1, a_2]$, with a_i uniformly distributed on $(0.7, 1.3)$ to reflect an assumed knowledge on the rough shape but without precise proportionality of the mass distribution[1]. As per Section 5.3, when kinematic priors are used with a 5% error from ground truth. Finally, as per Section 2.1, attitude and position estimations with errors proportional to the works [15, 35] are used; the measurement noise is observable in Figures 6 and 7.

Evaluation Metrics

The two metrics can be applied to internal filter parameters or state estimation variables. A visualization of the metrics is shared in Fig. 5. Tracking the error of the state estimation variables is intuitive (e.g., is the attitude, q_i, sufficiently close to the ground-truth). However, the error covariance matrix, P, (recall Eq. (16)) is a real-time estimate of the filter's uncertainty and thus useful for comparing differently tuned filters. Consider one filter, F_f, tuned for a *fast* angular velocity condition and a second filter, F_s, tuned for a *slow* angular velocity condition. If both F_f and F_s are tested on the slow angular velocity condition, F_f will likely converge faster than F_s (good), but F_f will likely exhibit a worse steady-state Root Mean Squared Error (RMSE) than F_s (bad). In such circumstance, it is thus beneficial to also observe the filters' error covariance matrices, P (i.e., do the F_f and F_s filters' confidence converge comparably and remain confident at steady state).

To evaluate the performance of the filters, two metrics are used

- **Convergence time** is defined as the time all tracked parameters pass below a set threshold and do not exceed the threshold again.
- **Steady state error** is defined as the RMSE of the parameters at steady state. Steady state is defined as from the convergence time to the end of the simulation.

[1] $\circ$ denotes the element-wise multiplication operation.

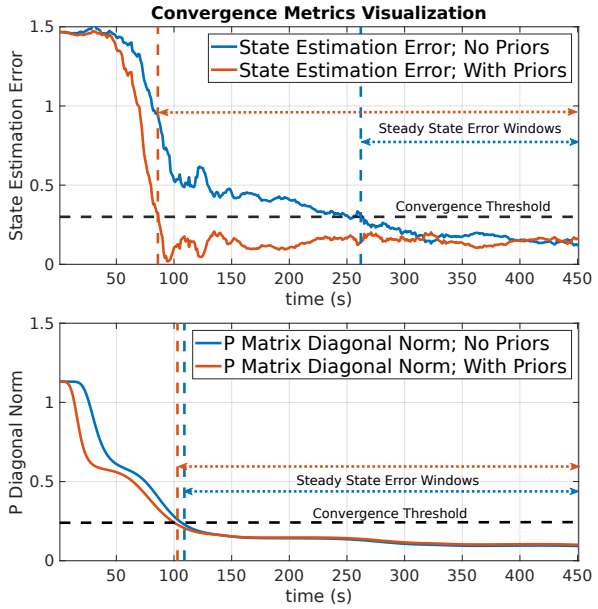

Figure 5. Convergence and Steady State Error Metrics [Top] using the state estimation error [Bottom] using the filter covariance matrix, P

Table 1. Scenarios definition, respectively: 1 axis slow/fast, 2-axes slow/fast

$\boldsymbol{\omega}$ $\frac{rad}{s}$	SC1 "slow"	SC2 "fast"	SC3 "slow"	SC4 "fast"
$\boldsymbol{\omega}_0^x$	0	0	0.020	0.100
$\boldsymbol{\omega}_0^y$	0	0	0	0
$\boldsymbol{\omega}_0^z$	0.050	0.200	0.045	0.150

6.1. Kalman Filter parameter tuning

For experiment 1, the availability of the motion prior is exploited to tune the process noise covariance matrix, Q_d, for a specific scenario. Four tumbling scenarios are defined in Table 1; two 1-axis tumbling conditions and two 2-axis tumbling conditions.

Tuning a single Kalman filter to perform optimally in every scenario is challenging. Assuming no motion prior information is available, the following tuning process is undertaken.

The process noise covariance matrix search space is quite large; it is recommended to increment through different orders of magnitude (e.g., $Q_1 = diag(10^0, 10^0, 10^0, ...)$, $Q_2 = diag(10^{-1}, 10^0, 10^0, ...)$, ...). The Kalman filter's score, $G_{KF}(i)$, is then used to identify the best filter for a given scenario. In the case that no kinematic priors are available, an engineer must conservatively tune the Kalman filter to accommodate all scenarios. The Kalman filter with the highest score for the SC4 2-axis fast tumble scenario (best $G_{KF}(4)$) is selected here as a conservative choice. Hereafter, KF_{gen} will refer to the generally tuned Kalman filter (no access to motion priors) and KF_{sc} will refer to the scenario specific tuned Kalman filter which exploits knowledge of the motion priors. Simulations are run for 300 s with a sampling time of 0.5 s (i.e, the pose estimation model acquires a new image every 1 second)

Algorithm 1 Q_d tuning process

Kalman Filter, KF
$Q_{parameters} = [Q_1, Q_2, ...Q_n]$
$SC = [SC1, SC2, SC3, SC4, ...]$

for Q in $Q_{parameters}$ **do**
  $KF \leftarrow Q$
  for i in $range(1, length(Scenarios))$ **do**
    Run Simulation $SC[i]$ with KF
    $SC[i] \rightarrow C_{t,i}$
    $SC[i] \rightarrow E_{SS,i}$
    $G_{KF}(i) = \lambda C_{t,i} + (1-\lambda)E_{SS,i}$
  end for
end for

Where,
C_t is the convergence time
E_{SS} is the RMSE at steady-state
λ is the bivariate weight
$G_{KF}(i)$ is the Kalman filter's "score" for a scenario

*Table 2. State based convergence time comparison for scenario specific tuning. The performance of the general tuned Kalman filter is shown in brackets. **Lower** times are better ↓. The scenario specific tuning outperforms the general tuning when the non bracketed number is **bold**.*

		SC1 [s]	SC2 [s]	SC3 [s]
UKF	$\boldsymbol{q}_{TS}$	73 (**22.0**)	36 (**34.0**)	**35** (**66.5**)
	$\boldsymbol{\omega}_{ST}$	4.0 (4.0)	5.5 (**4.5**)	4.0 (4.0)
	$\boldsymbol{r}_{ST}$	6.0 (**3.5**)	6.0 (**3.5**)	9.5 (**3.5**)
	$\boldsymbol{v}_{ST}$	5.5 (**4.0**)	5.5 (**4.0**)	7.5 (**4.0**)
	$\boldsymbol{J}_T^k$	- (-)	- (-)	281.0 (**108.5**)
EKF	$\boldsymbol{q}_{TS}$	56.5 (**20.0**)	**84.5** (114.5)	**37.0** (38.5)
	$\boldsymbol{\omega}_{ST}$	7.0 (7.0)	7.5 (7.5)	7.0 (7.0)
	$\boldsymbol{r}_{ST}$	10.5 (**5.5**)	6.0 (**5.5**)	10.5 (**5.5**)
	$\boldsymbol{v}_{ST}$	12.0 (**9.0**)	11.5 (**8.5**)	11.5 (**9.0**)
	$\boldsymbol{J}_T^k$	- (-)	- (-)	270 (**224.5**)

The KF_{gen}, KF_{sc} convergence comparison results are shared in Table 2 and the steady state error results are shared in Table 3. Note that the scenario 4 comparison is excluded from the tables as $KF_{gen} = KF_{sc}$. Additionally note that the inertia matrix, $\boldsymbol{J}_T^k$, is not estimated for scenario 1 and 2, as they are 1-axis torque free scenarios and thus independent of the inertia matrix.

Notably, the tuning of the KF_{sc} prioritized minimizing the steady state error. Consequently, the scenario convergence times showcased in Table 2 are similar, but with

*Table 3. State based steady state error comparison for scenario specific tuning. The performance of the general tuned Kalman filter is shown in brackets. **Lower** errors are better ↓. The scenario specific tuning outperforms the general tuning when the non bracketed number is **bold**.*

	$\times 10^{-3}$	SC1 [RMSE]	SC2 [RMSE]	SC3 [RMSE]
UKF	$\boldsymbol{q}_{TS}$	**723** (1123)	**771** (996)	1393 (**1198**)
	$\boldsymbol{\omega}_{ST}$	**3** (4)	5 (5)	5 (**4**)
	$\boldsymbol{r}_{ST}$	**323** (415)	**346** (422)	**283** (416)
	$\boldsymbol{v}_{ST}$	**132** (282)	**178** (303)	**91** (282)
	$\boldsymbol{J}_T^k$	- (-)	- (-)	1741 (**1737**)
EKF	$\boldsymbol{q}_{TS}$	**517** (944)	**619** (943)	**960** (1032)
	$\boldsymbol{\omega}_{ST}$	2 (2)	3 (3)	2 (2)
	$\boldsymbol{r}_{ST}$	**260** (323)	331 (**330**)	**252** (324)
	$\boldsymbol{v}_{ST}$	**57** (126)	**459** (460)	**64** (127)
	$\boldsymbol{J}_T^k$	- (-)	- (-)	**125** (1261)

generally worse performance of the KF_{sc} at converging to the correct attitude ($\boldsymbol{q}_{TS}$).

However, the KF_{sc} reduction in steady state error is significant and consistent across all scenarios as seen in Table 3. In particular, the EKF_{sc} exhibited a 10× reduction in steady state error while tracking the inertia matrix for scenario 3. It is clear that with access to kinematic priors it is possible to greatly reduce the steady state error of the Kalman filter for specific scenarios.

6.2. Inertia matrix estimation

For the second study, the scenario specific tuned Kalman Filter, KF_{sc}, for scenario 3 (2-axis slow tumbling) is considered. Simulations are run for 450 s with a sampling time of 1 s (i.e, the pose estimation model acquires a new image every 1 second). The kinematic prior (with a 5% error as per Section 5.3) is then injected as an initial condition for the angular velocity, $\hat{\omega}_0$. At the same time the values of the error covariance matrix, P_0, corresponding to rotation rate are initialized to a lower value, encouraging the filter to trust the initial condition.

The convergence time comparison and steady state error comparison are shown in Table 4 and Table 5 respectively. The metrics are calculated for both the state estimation variables and the filter error covariance matrix, P. Note that the rotation rate, $\boldsymbol{\omega}_{ST}$, convergence time is 0 s because the kinematic prior initial condition; $\boldsymbol{\omega}_{ST}$ starts converged and rise above the 2° threshold. Additionally, comparison plots of the no prior and with kinematic priors injected filters' error as a function of time are provided in Figure 6.

In the context of the EKF, the results show how the trust in the kinematic prior initial condition is able to shift the energy of the estimation process towards the inertia matrix component, $\boldsymbol{J}_T^k$. This is observable in both the state

*Table 4. Convergence time comparison for no prior and with kinematic prior injected. A **lower** convergence time [s] is better ↓. NaN indicates the filter did not converge below the set threshold.*

		UKF	+prior	EKF	+prior
State Based	$\boldsymbol{q}_{TS}$	NaN	NaN	**39**	90
	$\boldsymbol{\omega}_{ST}$	60	**0**	32	**0**
	$\boldsymbol{r}_{ST}$	176	176	176	176
	$\boldsymbol{v}_{ST}$	119	119	266	266
	$\boldsymbol{J}_T^k$	NaN	NaN	262	**86**
Filter Based	$\boldsymbol{q}_{TS}$	101	**85**	91	**37**
	$\boldsymbol{\omega}_{ST}$	74	**70**	49	**30**
	$\boldsymbol{r}_{ST}$	10	**8**	12	12
	$\boldsymbol{v}_{ST}$	9	**7**	13	13
	$\boldsymbol{J}_T^k$	121	**115**	109	**103**

*Table 5. Steady state error comparison for no prior and with kinematic prior injected. A **lower** RMSE is better ↓. NaN indicates the filter did not converge below the set threshold.*

	$\times 10^{-3}$	UKF	+prior	EKF	+prior
State Based	$\boldsymbol{q}_{TS}$	NaN	NaN	1466	**1288**
	$\boldsymbol{\omega}_{ST}$	4	4	**1**	2
	$\boldsymbol{r}_{ST}$	392	392	391	391
	$\boldsymbol{v}_{ST}$	101	**99**	108	**107**
	$\boldsymbol{J}_T^k$	NaN	NaN	184	**145**
Filter Based	$\boldsymbol{q}_{TS}$	2950	**2584**	**1275**	1949
	$\boldsymbol{\omega}_{ST}$	4	**3**	1	1
	$\boldsymbol{r}_{ST}$	401	**397**	395	395
	$\boldsymbol{v}_{ST}$	119	**101**	116	**115**
	$\boldsymbol{J}_T^k$	1181	**701**	310	**146**

estimation and filter metrics but is especially evident for the EKF, with a state variable convergence time reduction of 3×. Additionally the EKF $\boldsymbol{J}_T^k$ steady-state error is much improved from 0.184 to 0.145.

In the context of the UKF, both the quaternion, $\boldsymbol{q}_{TS}$, and inertia matrix, $\boldsymbol{J}_T^k$, estimations did not converge within the simulation time (with or without kinematic priors). An overall conclusion is that the UKF is slightly more unstable and some of its results do not exactly follow the expected trend obtained with the EKF.

6.3. Enhanced outlier rejection

For the third study, the scenario specific tuned Kalman Filter, KF_{sc} from study 1 is used. Additionally the kinematic priors are introduced as an initial condition as in study 2. Finally, the kinematic priors are lastly again exploited, not for outlier rejection. The kinematic prior

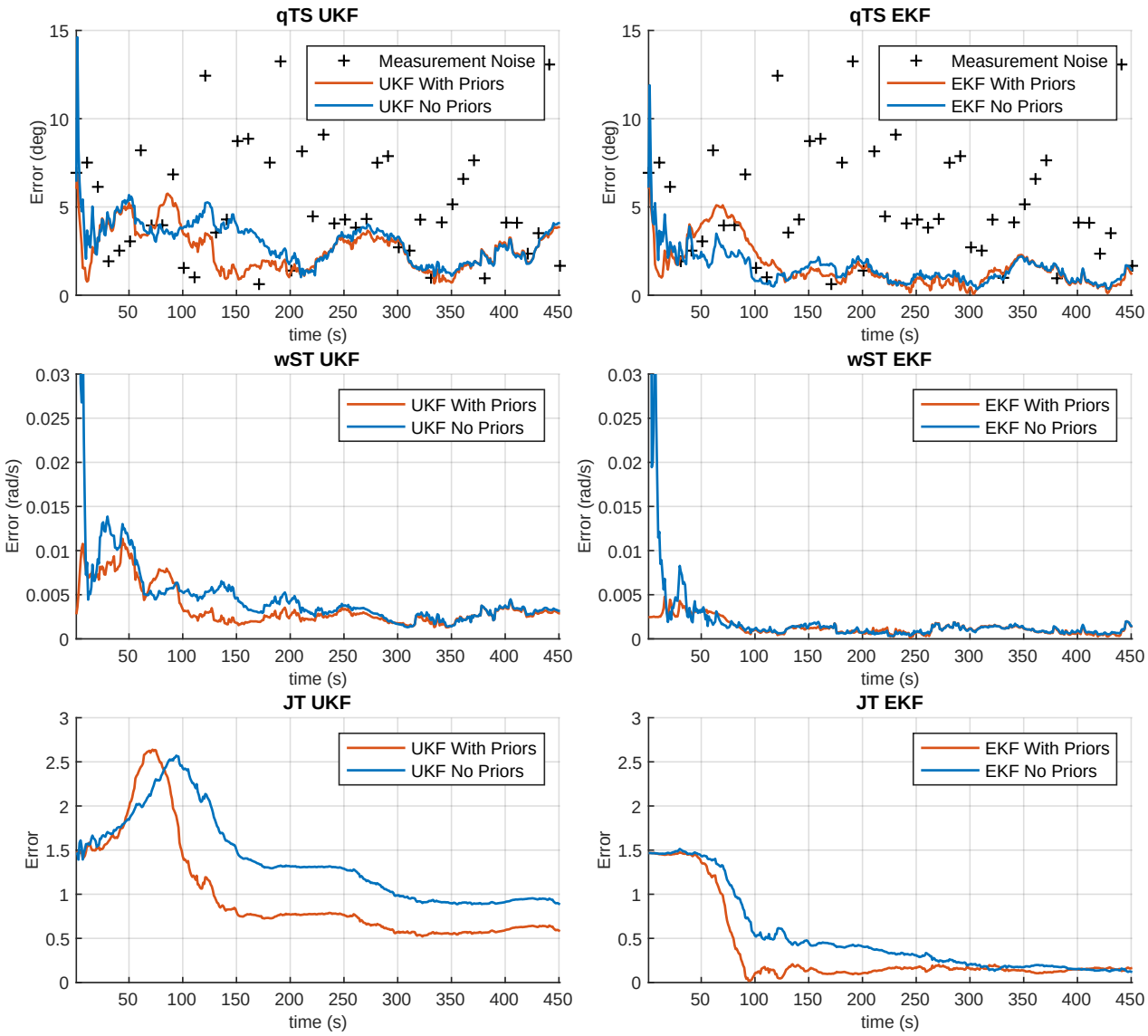

Figure 6. Relative attitude $\mathbf{q}_{TS}$, relative angular velocity ω_{ST}^{T} and target inertia matrix parameters $k_1^{J_T}, k_2^{J_T}$ estimation errors for a 2-axis slow tumbling scenario.

can firstly be used to establish an outlier rejection threshold (i.e., if an incoming measurement is outside what is expected, it is rejected). Secondly, if a measurement is rejected, the kinematic prior can be injected as a proxy measurement.

As discussed in Section 4.3, outlier/fault rejection can be an intricate process dependent on the source and length of the measured fault. For this study, redundancy is introduced to the measured state variables (attitude, $\boldsymbol{q}_{TS}$, and position, $\boldsymbol{r}_{ST}$). An additional measurement source is added to the state vector: the kinematic prior is "pushed" at each time step as a fixed fictitious measurement. Moreover, since each measurement needs to be weighted by a component on the R_d measurement noise matrix, an additional component $R_\omega = 10^{-3}[1 \quad 1 \quad 1]$ is defined to weight the forced kinematic prior measurement inside the Kalman filter. This implementation only supports a kinematic prior of a constant value (i.e., phase is not accounted for) and is therefore only applicable for 1-axis rotation.

The considered scenario is 1-axis slow tumbling. Simulations are run for 300 s with a sampling time of 1 s (i.e., the pose estimation model acquires a new image every 1 second). Kinematic prior error and measurement error are mainted from previous studies. A fault window of 120 s is simulated for both attitude, $\boldsymbol{q}_{TS}$, and position, $\boldsymbol{r}_{ST}$ measurements; such circumstance may be representative of a VBN system passing through an eclipse.

Steady state error values are shared in Table 6 with a 30 s settling time after the fault is finished to allow reconvergence. There is very marginal change in the steady state error with or without enhanced outlier rejection. The exception is in the UKF attitude, $\boldsymbol{q}_{TS}$, estimation. The fil-

*Table 6. Steady state error comparison for no prior and with kinematic prior enhanced fault rejection. A **lower** RMSE is better ↓.*

	$\times 10^{-3}$	UKF	+prior	EKF	+prior
State Based	$\boldsymbol{q}_{TS}$	12.50	**4.92**	**3.75**	4.88
	$\boldsymbol{\omega}_{ST}$	0.01	**0.00**	0.00	0.00
	$\boldsymbol{r}_{ST}$	42.69	42.69	39.90	**39.89**
	$\boldsymbol{v}_{ST}$	1.48	1.48	1.55	1.55
	$\boldsymbol{J}_T^k$	-	-	-	-

ters behave quite similarly after recovering from the fault. It is clear that the kinematic prior enhanced outlier rejection has a sufficiently relevant impact only in the attitude, $\boldsymbol{q}_{TS}$, and angular velocity, $\boldsymbol{\omega}_{ST}$, state estimations.

Comparison plots of the no prior and with kinematic prior enhanced outlier rejection filters' error as a function of time are provided in Figure 7. Notably, the enhanced outlier rejection greatly reduces the divergence of the angular velocity estimation, $\boldsymbol{\omega}_{ST}$. Moreover, a dramatic reduction in the attitude, $\boldsymbol{q}_{TS}$, estimation error is observed for the UKF. Conversely, a slightly worse attitude, $\boldsymbol{q}_{TS}$, estimation error is observed for the EKF.

Although not observable in Figure 7, the position, $\boldsymbol{r}_{ST}$, faults introduced a large but non-diverging error. In the event of a position fault, the attitude, $\boldsymbol{q}_{TS}$, and angular velocity, $\boldsymbol{\omega}_{ST}$, estimations are not significantly effected.

7. CONCLUSIONS

This work explored the enhancement of uncooperative spacecraft kinematic state estimation by leveraging kinematic priors extracted from light curves.

The simulation and state estimator's relative spacecraft dynamics model were first introduced. Two Kalman filter models enforcing the quaternion unitary norm constraint were then implemented; an EKF and a UKF. A discussion on light curve analysis justified the source and fidelity of the kinematic motion priors. Kinematic motion prior extraction was demonstrated on synthetic and commercial 1-axis tumbling data. Three orthogonal studies were performed to demonstrate the impact of injecting information from kinematic priors into the Kalman filter.

By exploiting kinematic priors, convergence time and steady state error reductions of $3\times$ or more are exhibited for certain state components, dependent on the kinematic scenario and filter tuning. Overall, the EKF outperformed the UKF. Notably, the UKF was quite sensitive to tuning and also unstable in challenging low sample rate conditions. If additional model nonlinearities (e.g., orbit perturbations, kinematic damping or atmosphere-induced torque) were considered, the environment would become intrinsically more challenging. Under such conditions, an UKF could conceivably outperform an EKF due to its improved handling of high nonlinearities.

This work has been developed in the context of a six months Master's Thesis project supervised by the EPFL Computer Vision Laboratory, hosted at the EPFL Space Center. Comprehensive mathematical and filter derivations are available in the Thesis manuscript.

7.1. Future work

Future efforts should be focused on easing the current assumptions.

First, model validation on higher precision synthetic data could be pursued. To this extent, orbital perturbations (e.g., Earth oblateness J2, third-body etc.) and dissipation torques (e.g., LEO atmospheric drag) in the attitude dynamics can be incorporated. Additionally, a Servicer's thrust model could be added to simulate realistic rendezvous operations.

Second, improved support for 2-axes tumbling scenarios could be developed. State-of-the-art light curve analysis and inversion techniques would enable more accurate motion prior extraction characterization for complex body tumbling around non-trivial axes. Consequently, the enhanced outlier rejection method in 6.3 could be extended for supporting multi-axes angular velocity injection.

ACKNOWLEDGMENTS

The authors would like to thank Luís Gonçalves for his invaluable collaboration and sharing his currently in development light curve simulator; we wish him success in the completion of his PhD. Additionally, the authors acknowledge the support of our industry partners ClearSpace, for providing access to high-fidelity data, and PAVE Space, for their valuable feedback on the applied relevance of this work. Finally, we thank EPFL CVLab for funding the participation in the 9^{th} European Conference on Space Debris.

REFERENCES

1. Belton, M. J.S. ; Julian, W. H. ; Jay, A. A.; Mueller, B. E.A. *The spin state and homogeneity of comet Halley's nucleus*, Icarus, Vol. 93, No. 2, 1991, pp 183-193

2. Blacketer, Laurence. *Attitude Characterisation of Space Objects Using Optical Light Curves*. PhD Thesis, University of Southampton, March 2022.

3. Burton, Alexander; Frueh, Carolin. *Fast Light Curve Inversion for Regular and Tumbling Attitude Motion*. Advanced Maui Optical and Space Surveillance Technologies Conference 2023.

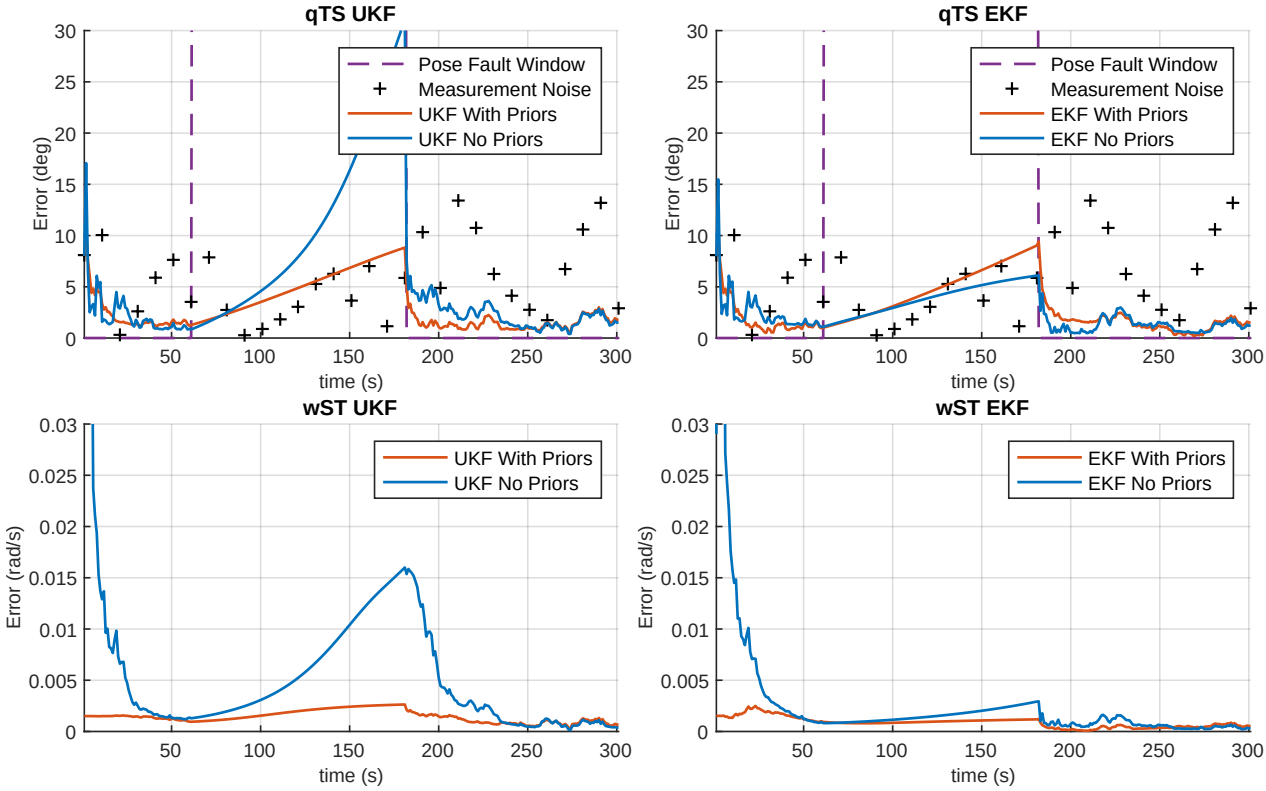

Figure 7. Relative attitude, $\mathbf{q}_{TS}$, and relative angular velocity, ω_{ST}^{T}, estimation errors.

4. Capuano, Vincenzo; Kim, Kyunam; Hu, Juliette; Harvard, Alexei; Chung, Soon-Jo. *Monocular-Based Pose Determination of Uncooperative Known and Unknown Space Objects*. International Astronautical Congress, 2018.

5. Chabot, Thomas; Kanani, Keyvan; Pollini, Alexandre; Chaumette, François; Marchand, Eric; Forshaw, Jason. *Vision-Based Navigation Experiment Onboard the RemoveDebris Mission*. 10th International ESA Conference on Guidance, Navigation and Control Systems. 29 May - 2 June 2017, Salzburg Austria.

6. Cook, R. L.; Torrance, K. E. *A Reflectance Model for Computer Graphics*. ACM Transactions on Graphics, Vol. 1, No. 1, pp. 7–24, January 1982.

7. Crassidis, John L.; Markley, F. Landis. *Unscented Filtering for Spacecraft Attitude Estimation*. Journal of Guidance, Control, and Dynamics, Vol. 26, No. 4, July 2003, pp. 536–542.

8. D'Amico, Simone; Benn, Mathias; Jørgensen, John. *Pose Estimation of an Uncooperative Spacecraft from Actual Space Imagery*. International Journal of Space Science and Engineering. Vol 2. No. 2. 2014. pp. 171 – 189.

9. Eyer, L. ; Mowlavi, N. *Variable stars across the observational HR diagram* Journal of Physics: Conference Series, vol. 118, 2008, p. 012010.

10. ESA Space Debris Office (2024). *ESA's Annual Space Environment Report (v8)*. ESA ESOC.

Eyer, L. ; Mowlavi, N. *Variable stars across the observational HR diagram*, Journal of Physics: Conference Series, Vol. 118, 2008, pp 012010

11. Forshaw, Jason; Aglietti, Gulielmo; Salmon, Thierry; Retat, Ingo; Roe, Mark; Burgess, Christopher; Chabot, Thomas; Pisseloup, Aurélien; Phipps, Andy; Bernal, Cesar; Chaumette, François, Pollini, Alexandre; Steyn, William. *Final payload test results for the RemoveDebris active debris removal mission*. Acta Astronautica Vol. 138. 2017. pp. 326–342.

12. Gurfil, Pini; Kholshevnikov, Konstantin V. *Manifolds and Metrics in the Relative Spacecraft Motion Problem*. Journal of Guidance, Control, and Dynamics, Vol. 29, No. 4, July 2006, pp. 1004–1010.

13. Hellmich, Stephan; Rachith, Elisabeth; Chang, Belén Yu Irureta-Goyena; Kneib, Jean-Paul. *Harvesting large astronomical data archives for space debris observations*. 2nd NEO and Debris Detection Conference. Darmstadt, Germany. January 2023.

14. Hirabayashi, Masatoshi; Tsuda, Yuichi. *Hayabusa2 Asteroid Sample Return Mission*. Elsevier Book. 2022. ISBN 978-0-323-99731-7.

15. Hu, Yinlin; Speierer, Sébastien; Jakob, Wenzel; Fua, Pascal; Salzmann, Mathieu. *Wide-Depth-Range 6D Object Pose Estimation in Space*. Computer Vision and Pattern Recognition 2021.

16. JAXA Press Release. *CRD2 Phase I / ADRAS-J Update: Fly-Around Observation Images of Space Debris Released*. July 30, 2024. JAXA.

17. Julier, Simon J.; Uhlmann, Jeffrey K. *New Extension of the Kalman Filter to Nonlinear Systems*. Signal Processing, Sensor Fusion, and Target Recognition VI, Vol. 3068, SPIE, July 1997, pp. 182–193.

18. Kaasalainen, M.; Torppa, J. *Optimization Methods for Asteroid Lightcurve Inversion: I. Shape Determination*, Icarus, Vol. 153, No. 1, 2001, pp 24-36

19. Kaasalainen, M.; Torppa, J., Muinonen, K. *Optimization Methods for Asteroid Lightcurve Inversion: II. The Complete Inverse Problem*, Icarus, Vol. 153, No. 1, 2001, pp 37-51

20. Kalman, R. E.; Bucy, R. S. *New Results in Linear Filtering and Prediction Theory*. Journal of Basic Engineering, Vol. 83, No. 1, March 1961, pp. 95–108.

21. Kisantal, M.; Sharma, S.; Park, T.H.; Izzo, D.; M artens, M.; D'Amico, S. *Satellite Pose Estimation Challenge: Dataset, Competition Design and Results*. IEEE Transactions on Aerospace and Electronic Systems. Vol. 56. No. 5. 2020. pp. 4083–4098.

22. Kim, Du Yong; Lee, Sang-Goog; Jeon, Moongu. *Outlier Rejection Methods for Robust Kalman Filtering*. In Park, James J.; Yang, Laurence T.; Lee, Changhoon (Eds.), *Future Information Technology*, Springer, 2011, pp. 316–322.

23. Meech, K. J.; Belton, M. J. S.; Mueller, B. E. A.; Dicksion, M. W.; Li, H. R. *Nucleus Properties of P/Schwassmann-Wachmann 1*, Astronomical Journal, Vol. 106, No. 3, 1991, pp 1222-1236

24. Miralda-Escudé, J. *Orbital Perturbations of Transiting Planets: A Possible Method to Measure Stellar Quadrupoles and to Detect Earth-Mass Planets*, The Astrophysical Journal, Vol. 564 No. 2, 2002, pp 1019

25. Mueller, B *The Diagnosis of Complex Rotation in the Lightcurve of 4179 Toutatis and Potential Applications to Other Asteroids and Bare Cometary Nuclei*, Icarus, Vol. 158, No. 2, 2002, pp 305-311

26. Oki, Yusuke; Yoshikawa, Kent; Takeuchi, Hiroshi; Kikuchi, Shota; Ikeda, Hitosi; Scheeres, Daniel J.; McMahon, Jay W.; Kawaguchi, Junichiro; Takei, Yuto; Mimasu, Yuya; Ogawa, Naoko; Ono, Go; Terui, Fuyuto; Yamada, Manabu; Kouyama, Toru; Kameda, Shingo; Yoshida, Kazuya; Nagaoka, Kenji; Yoshimitsu, Tetsuo; Saiki, Takanao; Tsuda, Yuichi. *Orbit insertion strategy of Hayabusa2's rover with large release uncertainty around the asteroid Ryugu*. Journal of Astrodynamics. Vol. 4. No. 4. 2020. pp. 309–329.

27. Oszkiewicz, D.A. ; Muinonen, K. ; Bowell, E. ; Trilling, D. ; Penttilä, A. ; Pieniluoma, T. ; Wasserman, L.H. ; Enga, M.-T. *Online multi-parameter phase-curve fitting and application to a large corpus of asteroid photometric data*, Journal of Quantitative Spectroscopy and Radiative Transfer, Vol. 112, No. 11, 2011, pp 1919-1929

28. Park, Tae Ha; D'Amico, Simone. *Adaptive Neural-Network-Based Unscented Kalman Filter for Robust Pose Tracking of Noncooperative Spacecraft*. Journal of Guidance, Control, and Dynamics, Vol. 46, No. 9, 2023, pp. 1671–1688.

29. Park, T.H.; M artens, M.; Jawaid, M.; Wang, Z.; Chen, B.; Chin, T.-J.; Izzo, D.; D'Amico, S. *Satellite Pose Estimation Competition 2021: Results and Analyses*. Acta Astronautica. Vol. 204. 2023. pp. 640-665.

30. Petit, A.; Rolin, A.; Duthil, L.; Tarrieu, H.; Lucken, R.; Giolito, D. *Extraction of Light Curves from Passive Observations during Survey Campaign in LEO, MEO and GEO Regions*. Advanced Maui Optical and Space Surveillance Technologies Conference 2022.

31. Plett, Gregory. *ECE5550: Applied Kalman Filtering*. Lectures ECE5550: Applied Kalman Filtering - University of Colorado, Colorado Springs.

32. Price, Andrew; Yoshida, Kazuya. *A Monocular Pose Estimation Case Study: The Hayabusa2 Minerva-II2 Deployment*. Computer Vision and Pattern Recognition AI4Space Workshop. Virtual. 2021.

33. Pyrak, Matt; Anderson, Joseph. *Performance of Northrop Grumman's Mission Extension Vehicle (MEV) RPO Imagers at GEO*. Advanced Maui Optical and Space Surveillance Technologies Conference 2021.

34. Rachith, Elisabeth; Hellmich, Stephan; Irureta-Goyena, Belén. *A Novel Machine Learning Based Algorithm for Efficient Streak Detection* . 2nd International Orbital Debris Conference. 4-7 December, 2023. Sugar Land, Texas.

35. Sajjad, Niki; Price, Andrew; Mirshams, Mehran; Salzmann, Mathieu. *Tiny satellites, big challenges: A feasibility study of machine vision pose estimation for PocketQubes during conjunctions*. Acta Astronautica. Vol. 228. 2025. pp. 1023–1041.

36. Šilha J., *Space Debris: Optical Measurements*, Reviews in Frontiers of Modern Astrophysics: From Space Debris to Cosmology, 2020

37. Suzuki, H.; Yamada, M.; Kouyama, T.; Tatsumi, E.; Kameda, S.; Honda, R.; Sawada, H.; Ogawa, N.; Morota, T.; Honda, C.; Sakatani, N.; Hayakawa, M.; Yokota, Y.; Yamamoto, Y.; Sugita, S. *Initial inflight calibration for Hayabusa2 optical navigation camera (ONC) for science observations of asteroid Ryugu*. Icarus. Vol. 300. 2018. pp. 341–359.

38. Tweddle, Brent E.; Saenz-Otero, Alvar. *Relative Computer Vision-Based Navigation for Small Inspection Spacecraft*. Journal of Guidance, Control, and Dynamics, Vol. 38, No. 5, May 2015, pp. 969–978.

39. Warner, Brian D.; Harris, Alan W. ; Pravec, Petr. *The asteroid lightcurve database*, Icarus, Vol. 202, No. 1, July 2009, pp. 134-146.